

Article

Performance Improvement of a High Loading Centrifugal Compressor with Vaned Diffuser by Hub Contour Optimization

Yunfeng Wu ^{1,2,3} , Qingkuo Li ⁴, Hang Yuan ^{1,2,3}, Ziliang Li ^{1,2,3}, Shiji Zhou ^{1,2,3}, Ge Han ^{1,2,3} and Xingen Lu ^{1,2,3,*}

¹ National Key Laboratory of Science and Technology on Advanced Light-Duty Gas Turbine, Chinese Academy of Sciences, Beijing 100190, China; wuyunfeng@iet.cn (Y.W.); yuanhang@iet.cn (H.Y.); liziliang1997@outlook.com (Z.L.); zhoushiji@iet.cn (S.Z.); hange@iet.cn (G.H.)

² Key Laboratory of Light-duty Gas-turbine/Institute of Engineering Thermophysics, Chinese Academy of Sciences, Beijing 100190, China

³ School of Aeronautics and Astronautics, University of Chinese Academy of Sciences, Beijing 100190, China

⁴ Department of Mechanical, Manufacturing and Biomedical Engineering, Trinity College Dublin, Parsons Building, College Green, D02 PN40 Dublin, Ireland; qli3@tcd.ie

* Correspondence: xingenlu@hotmail.com

Abstract: High-pressure ratio centrifugal compressors' diffusers face challenges from high-velocity, non-uniform flow at the impeller outlet, decreasing efficiency and stall margin. To address this, this paper presents a novel vaned diffuser passage design method that successfully improved the compressor's performance. An optimization method using axisymmetric hub contours and NURBS curves was applied to modify the diffuser's design. After optimization, centrifugal compressor peak efficiency increased by 0.78%, and stall margin expanded from 12.8% to 20.4%. Analysis at the peak efficiency point showed loss reduction mainly from decreased recirculation and mixing losses in the diffuser's vaneless and semi-vaneless spaces. Furthermore, correlation analysis and Mach number distribution revealed that flow behavior at the diffuser's leading edge significantly influences efficiency. Consequently, design principles emphasize satisfying specific Mach number distribution rules at the diffuser's leading edge under certain inflow conditions for optimal performance.

Keywords: high-loading centrifugal compressor; aerodynamic optimization; axisymmetric hub contour; wedge diffuser; entropy loss



Citation: Wu, Y.; Li, Q.; Yuan, H.; Li, Z.; Zhou, S.; Han, G.; Lu, X. Performance Improvement of a High Loading Centrifugal Compressor with Vaned Diffuser by Hub Contour Optimization. *Aerospace* **2024**, *11*, 246. <https://doi.org/10.3390/aerospace11040246>

Academic Editors: Andrea Magrini and Ernesto Benini

Received: 21 February 2024

Revised: 16 March 2024

Accepted: 19 March 2024

Published: 22 March 2024



Copyright: © 2024 by the authors. Licensee MDPI, Basel, Switzerland. This article is an open access article distributed under the terms and conditions of the Creative Commons Attribution (CC BY) license (<https://creativecommons.org/licenses/by/4.0/>).

1. Introduction

Centrifugal compressors are extensively utilized across diverse industries due to their high single-stage pressure ratio, operational stability, and compact structure. These machines find extensive applications in metallurgy, chemical engineering, petrochemical engineering, refineries, natural gas and pipeline industries, refrigeration, armored vehicles, automotive power units, and small aviation engines [1,2]. Centrifugal compressors require improved aerodynamic performance and a broad operating range. Centrifugal compressors with a single-stage pressure ratio exceeding 5:1 have an impeller exit characterized by supersonic flow and high non-uniformity. Consequently, the diffusion section of these machines encounters significant challenges. Typically, the velocity of this non-uniform supersonic flow is reduced by a factor of 8 in the diffuser, leading to substantial losses. Hence, investigating the flow process in the diffuser is a crucial aspect of any research program focused on centrifugal compressors [3].

The initially utilized vaneless diffuser, due to its simplistic structural design, was extensively employed. Its diffusion capability depends on the diameter of its outlet. However, as the pressure ratio of the centrifugal compressor increases, vaneless diffusers with a radius ratio exceeding 2 are no longer favored due to significant frictional losses associated with elongated diffusers. Additionally, the increase in radial length results in only negligible enhancement in pressure recovery [4]. The introduction of vaned diffusers

improves pressure recovery and reduces losses for radial diffusers with identical radius ratios, although it limits the operating range of the compressor. Consequently, researchers have dedicated considerable effort to enhancing compressor efficiency and broadening its operational envelope. Yoshinaga [5] conducted exhaustive experiments on 16 distinct vaned diffusers using a model compressor test rig, revealing a critical diffusion ratio that corresponded to a notable surge in diffuser pressure recovery. Abdelwahab [6] proposed a three-dimensional vaned diffuser characterized by varying solidity and stagger angles along the spanwise direction, combining the broad operating range of low-solidity diffusers with the high performance characteristics of high-solidity diffusers. Issac [7] systematically investigated the heights of diffuser vanes and conducted comparative studies by fixing partial vanes on the hub or shroud. Remarkably, fixing partial vanes at half spacing offset on the hub and casing resulted in significant improvements in compressor performance.

Early investigations into axisymmetric endwall contouring primarily focused on turbine applications, aiming to reduce secondary vortex size and intensity by locally contracting the flow area within the turbine. This contraction aimed to minimize losses associated with these vortices [8–14]. In compressors, axisymmetric endwall contouring serves two primary purposes. First, it aims to improve flow near the endwall during near-stall conditions, significantly enhancing the compressor's stall margin [15]. Secondly, it seeks to enhance the flow structure by mitigating blade tip leakage flow [16,17], controlling boundary layer flow along the endwall [18], and reducing corner separation [19]. The ultimate goal is to minimize losses and enhance the overall performance of the compressor. Sun's research [20] explored various axisymmetric endwall profiles for transonic rotors. These profiles were found to impact shock structures, subsequently altering the compressor's loss distribution and operating range. However, research on the application of axisymmetric endwall contouring in radial diffusers is limited. The impact of axisymmetric endwall contouring on centrifugal compressor diffuser flow, and its potential to enhance performance and expand operating range, remains underexplored. Although design insights from axial compressors can provide some guidance, the non-uniform circumferential and axial heights at the impeller exit in high-pressure ratio centrifugal compressors present more challenging inflow conditions for the diffuser. Therefore, a more detailed discussion is necessary to elucidate axisymmetric endwall contouring's impact on the internal flow of centrifugal compressors [21].

In recent years, the development of optimization methods has accelerated due to advances in computer technology. Numerous studies have utilized various optimization techniques to optimize compressor design parameters, such as meridional passage, blade shape, and casing treatment configuration [22–29]. These studies have significantly enhanced compressor performance and expanded its operational range. Consequently, this study used the multi-objective particle swarm optimization (MOPS) algorithm to optimize axisymmetric endwall contouring in the diffuser, aiming primarily to enhance compressor performance. Following the implementation of endwall contouring, a comprehensive analysis of the diffuser's internal flow and a thorough examination of the underlying reasons for performance improvements were conducted. To understand the factors contributing to performance changes holistically, the diffuser was divided into smaller subsections. Internal flow losses were systematically categorized, followed by a quantitative assessment of loss variations in each subsection. Furthermore, this paper summarizes Mach number (Ma) variations in the diffuser, leading to the identification of design principles for endwall contouring suitable for specific inflow conditions, based on the radial distribution of Ma.

2. Research Model and Methodology

This study focuses on a high-pressure ratio centrifugal compressor with a compact structure, featuring a single impeller with splitter blades and a wedge diffuser, as shown in Figure 1. Table 1 presents an overview of the compressor's essential parameters.

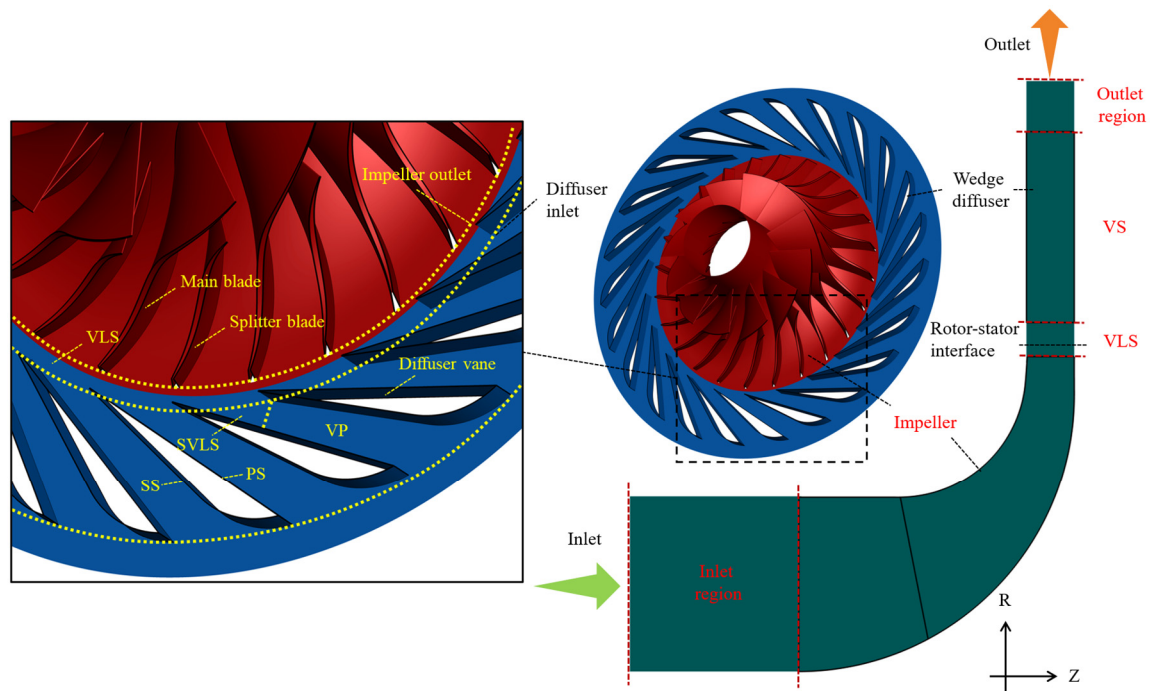


Figure 1. Schematic view of the object compressor.

Table 1. Main compressor parameters.

Parameter	Value
Design mass flow rate	1.51 kg/s
Design total pressure ratio	5.9
Impeller	
Number of blades	12 + 12
Design rotating speed	65,000 rpm
Tip radial clearance	0.15 mm
Inlet diameter	112 mm
Outlet diameter	162 mm
Wedge diffuser	
Number of blades	23
Inlet diameter	174 mm
Outlet diameter	242 mm
Blade height	8.5 mm

A non-uniform rational B-spline (NURBS) curve was used to shape the hub contour. This choice was motivated by its flexibility and the convenience of associated algorithms, facilitating implementation on computer systems. These characteristics perfectly align with the diffuser hub contour design requirements outlined in this paper. Initially, the baseline hub contour is depicted as a straight-line segment. To define the hub contour, 10 control points are strategically placed. In the R–Z coordinate system, a single degree of freedom is assigned, with the R coordinate constant and only the Z coordinate varying. Table 2 details the distribution of the R coordinates for these 10 control points. Specifically, the ratio of the radius at Control Point 1 (R1) to the impeller outlet radius is 1.025, while R10 matches the exit radius of the diffuser stage. Normalization was applied to standardize distances between control points 1 and 10. To ensure proper radial inflow and outflow in the diffuser, control points are densely concentrated near the inlet and outlet. Notably, the inlet region requires particular attention because its flow dynamics critically affect the overall compressor stage performance [30–33]. Therefore, control points in this area were deliberately placed at a higher density. Control points in the middle section of the diffuser are uniformly distributed. The resulting sculpted hub contour is shown in Figure 2.

Table 2. Control point settings for hub contouring.

Control Point Number	1	2	3	4	5	6	7	8	9	10
R	0	0.05	0.1	0.2	0.35	0.5	0.65	0.8	0.95	1
Z	0	0	Var1	Var2	Var3	Var4	Var5	Var6	Var7	Var7

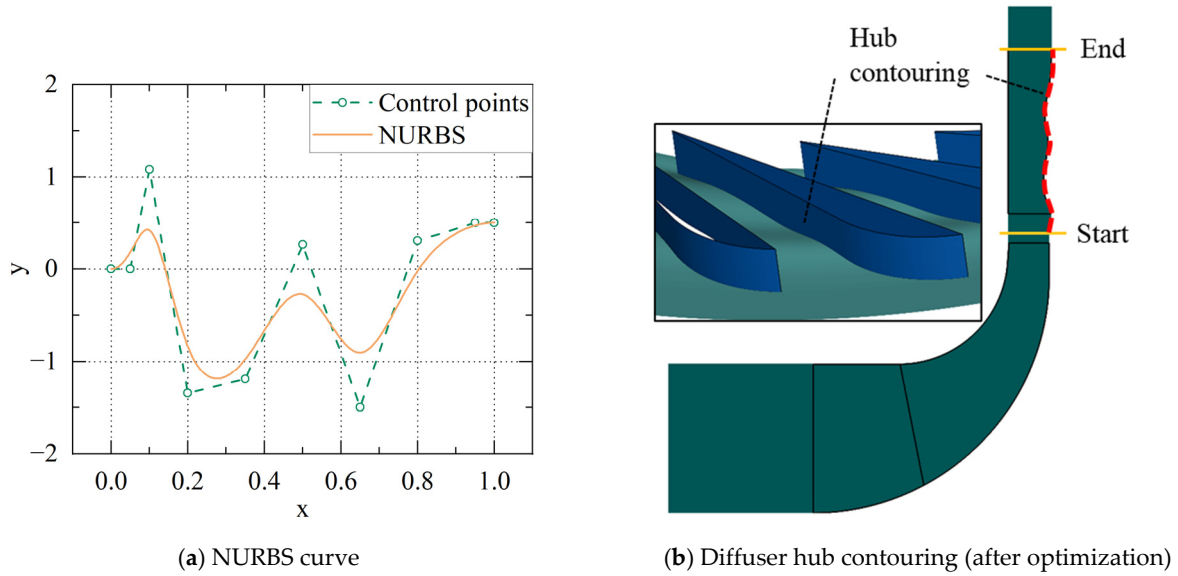


Figure 2. Schematic view of NURBS curves and diffuser hub contouring.

Three-dimensional steady simulation calculations for a single-stage rotor and stator channel were conducted via NUMECA Fine Turbo, using the Spalart–Allmaras model. The computational domain included periodic boundary conditions circumferentially and no-slip wall conditions on the solid wall. Inlet conditions were set to a total temperature of 288.15 K and a total pressure of 101,325 Pa, with axial inflow. Outlet conditions were defined as average static pressure. NUMECA Auto Grid5 was used for grid generation. The first-layer cell size on the wall surface was set to 0.001 mm to ensure most Y^+ values for the first-layer grids on the wall were below 2. Grid independence was verified, with results shown in Figure 3. The final grid cell count was 3.1 million, with 2.3 million mesh cells for the impeller and 0.8 million for the diffuser. Figure 4 presents detailed illustrations of the grid layout.

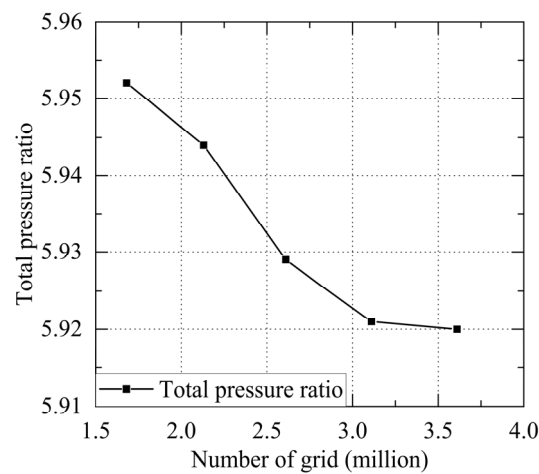


Figure 3. Results of the grid independence test.

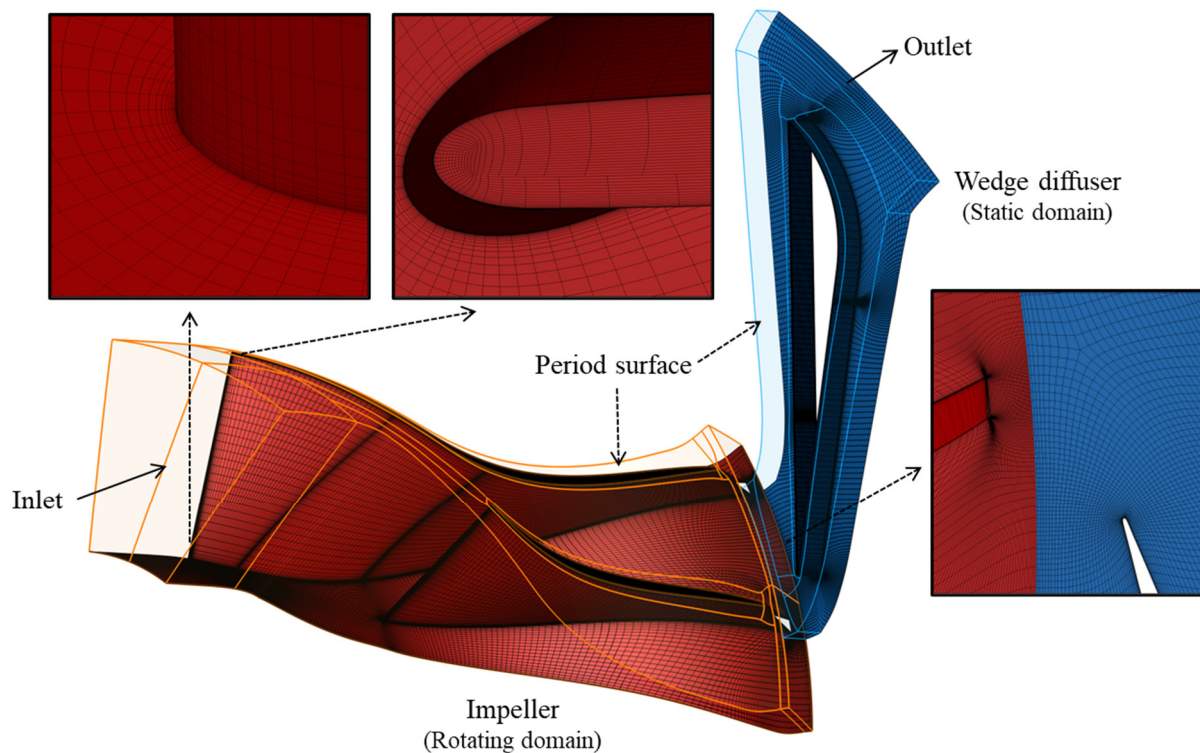


Figure 4. Illustration of the grid and computational domain.

The experimental test rig used in this study was established by the Institute of Engineering Thermophysics, Chinese Academy of Sciences. The rig consists of two parts: the compressor cycle and the turbine cycle. Airflow enters the compressor through a trumpet mouth and a rectification section without pre-swirl and then discharges into the environment through a volute. The compressor's operational conditions are precisely regulated by a downstream throttle valve, enabling precise control over the outlet static pressure. The rotor of the compressor is driven by the turbine. The turbine cycle includes an additional compressor for gas compression, a combustion chamber for energy generation, and a turbine for power output. This apparatus allows flexible modulation of rotational speeds within the range of 0–65,000 revolutions per minute (rpm), with a minimal speed deviation of approximately $\pm 0.15\%$. Calibrated double-twist flowmeters, positioned strategically at the compressor inlet, accurately measure mass flow rate with a relative error margin of $\pm 0.5\%$. Piezoelectric pressure sensors and thermocouples are used to collect comprehensive data on total pressure and total temperature, enabling performance calculations. At the compressor inlet, a radial three-point rake total pressure probe is placed at 120° circumferential location to measure the total pressure. The measurement points are located radially at 66 mm, 75.5 mm, and 83.9 mm, respectively. Additionally, a static pressure probe placed at 0° circumferential location gauges wall static pressure, and a radial three-point rake total temperature probe is placed at 240° circumferential location to measure the total temperature. The radial distribution of the temperature probe measurement points is the same as the total pressure probe. At the outlet, total pressure is measured by two axial three-point rake total pressure probes placed at 180° and 300° circumferential locations, respectively, and the measurement points are located radially at 130 mm. Static pressure is measured by a static pressure probe near the shroud at 30° circumferential location. Total temperature is measured by two radial three-point rake total temperature probes which are placed at 120° and 240° circumferential locations respectively, and the measurement points are also located radially at 130 mm. Crucially, error propagation analysis is applied to calculate the measurements, yielding a total pressure ratio error rate of approximately $\pm 0.3\%$ and an isentropic efficiency error margin of approximately $\pm 1\%$. Furthermore, to represent the experiment's performance characteristics, corrections to the speed and flow rate values

have been made. Notably, at the specified inlet Reynolds number, the compressor's performance consistently falls within the self-modelling region, as previous studies [34,35] have determined. Finally, Figure 5 shows the agreement between the experimental findings and the numerical simulations, demonstrating the efficacy and reliability of the numerical methodologies used in this research.

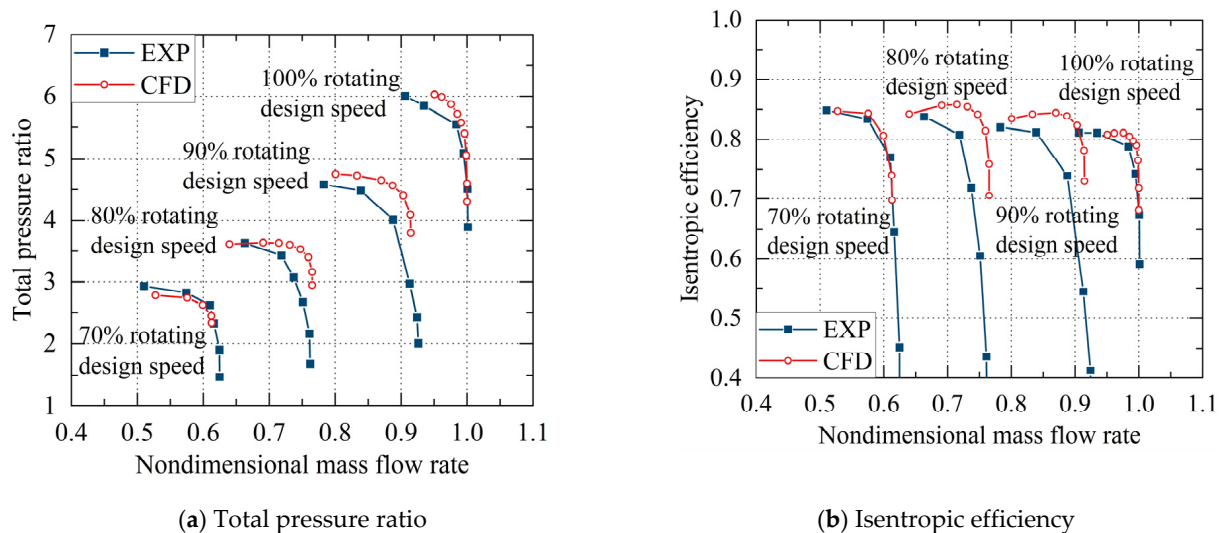


Figure 5. Comparison of the baseline compressor performance characteristic between the numerical calculations and experiments.

Multi-objective particle swarm optimization (MOPSO) optimizes calculations by mimicking the social behavior of animal groups, like flocks of birds or fish shoals. Finding an optimal design point resembles the food-foraging activity of these organisms. Particle swarm optimization is a population-based search procedure where individuals (called particles) continuously change position (called state) within the search area. In simpler terms, particles 'fly' through the design space to find the best position. The particle's next position is determined by the best position it and its neighbors encounter, along with its current velocity and inertia. For this study, the "maximum iterations" was set to 30, and the "number of particles" at 10. A total of 10 control points were named Control Point 1 to Control Point 10. The first two control points had a z-coordinate fixed at 0 to align the diffuser inlet with the impeller outlet. The last control point's z-value matched Control Point 9, creating a parallel hub and shroud at the diffuser outlet to facilitate radial outflow. Thus, a total of 7 variables are needed, as detailed in Table 2. The variables can vary by ± 1.5 mm, accounting for about 35% of the diffuser's vane height. The optimization objective is to achieve higher peak efficiency while maintaining flow rate, static pressure rise, and total pressure rise. This optimization aims to improve peak operating point efficiency with minimal changes to mass flow rate and the diffuser's pressure recovery capacity. The baseline mass flow rate at the peak efficiency point was 1.513 kg/s, with an efficiency of 81.12% and a pressure ratio of 6.029.

3. Discussion of Numerical Results

3.1. Comparison of Performance

Figure 6 depicts the performance characteristics before and after optimization. Mass flow rate values have been normalized using their respective choke mass flow rates for dimensionless representation. After optimization, significant improvements in efficiency and pressure ratio at the peak operating point were observed. Specifically, efficiency improved notably by 0.78%. Furthermore, the stall margin of the baseline, initially 12.8%,

expanded to 20.4% after optimization, a remarkable increase of 7.6%. The margin, indicative of operational stability, was calculated using Equation (1):

$$SM = \left(\frac{\pi_{\text{stall}}/m_{\text{stall}}}{\pi_{\text{design}}/m_{\text{design}}} - 1 \right) \times 100\% \quad (1)$$

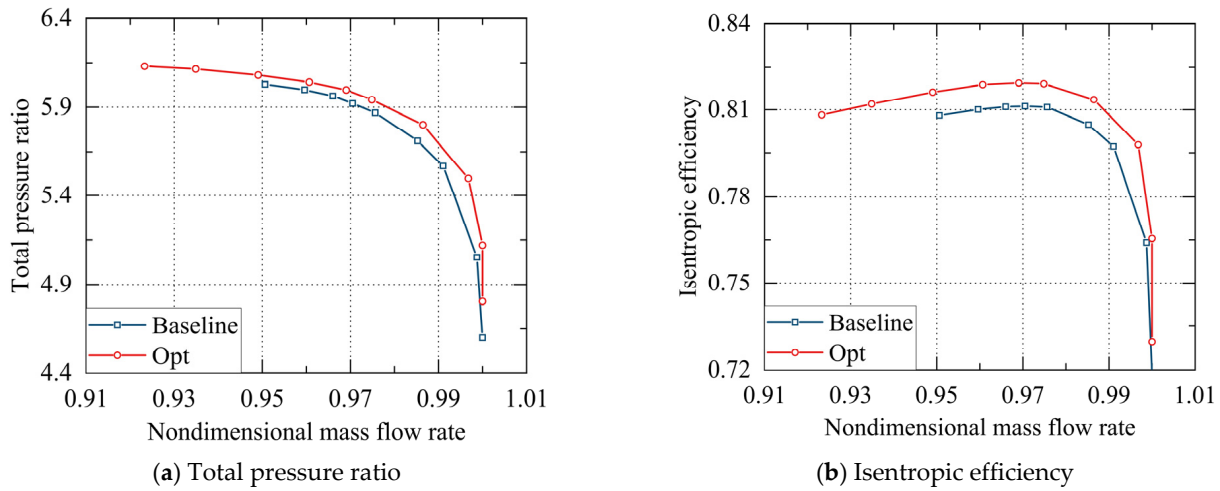


Figure 6. Comparison of the compressor performance characteristic between baseline and optimization.

Compared with the baseline, the reduction in choke mass flow rate was about 0.5%, as shown by Equation (2). This decline is primarily due to the optimized diffuser's throat area. In the centrifugal compressor stage's original design, the throat was located at the diffuser's narrowest region. As the static pressure at the compressor outlet gradually decreases to a threshold, a shock wave initially forms at the diffuser throat. Even with further reduction in outlet static pressure, downstream perturbations cannot propagate upstream across the diffuser throat, establishing a definitive choke. After optimization, the hub profile of the diffuser is elevated at the throat location, causing channel contraction and a consequent reduction in throat area compared with the baseline. Consequently, this reduced flow capacity leads to a lower flow rate at the choke point.

$$MC = \frac{m_{\text{Baseline,choke}} - m_{\text{Opt,choke}}}{m_{\text{Baseline,choke}}} \times 100\% \quad (2)$$

As defined by Equation (3), compressor efficiency is the ratio of isentropic work to actual work performed. This relationship can be expressed through total temperature and total pressure values. Thus, compressor isentropic efficiency is mainly influenced by two factors: the total pressure ratio and the total temperature ratio at the inlet and outlet. Therefore, the total pressure ratio indicates isentropic work, and the total temperature ratio indicates actual work accomplished. At the peak efficiency point of the baseline case, the optimized compressor shows an increased total pressure ratio and a decreased total temperature ratio under identical flow conditions. This implies that the optimized compressor not only enhances its functional capabilities but also mitigates actual losses. For a compressor, these scenarios are desirable objectives for designers to pursue. Moreover, in a cyclic system like an aircraft engine, a higher total pressure ratio in the compressor improves overall system efficiency.

$$L_{\text{ideal}} = \frac{k}{k-1} RT_{\text{in}} \left[\left(P_{\text{t,out}}/P_{\text{t,in}} \right)^{\frac{k-1}{k}} - 1 \right]$$

$$L_{\text{actual}} = \frac{k}{k-1} RT_{\text{in}} [T_{\text{t,out}}/T_{\text{t,in}} - 1]$$

$$\eta = \frac{L_{ideal}}{L_{actual}} = \frac{(P_{t,out}/P_{t,in})^{\frac{k-1}{k}} - 1}{T_{t,out}/T_{t,in} - 1} \quad (3)$$

The centrifugal compressor consists of three distinct components: the impeller, the vaneless space (VLS) region of the diffuser, and the vane space (VS) region of the diffuser. A thorough analysis before and after optimization elucidates each component's impact on efficiency and total pressure ratio. Figure 7 shows significant performance improvements in all three components of the optimized compressor. The impeller, a work-generating component, has its performance gauged primarily by efficiency. After optimization, the impeller's efficiency improves markedly across all conditions, especially at lower flow conditions with a 0.2% increase. Conversely, the vaneless and vane space regions of the diffuser are static components, with performance assessed via the total pressure loss coefficient, as outlined in Equation (4). After optimization, the vaneless space region of the diffuser shows a notable decline in total pressure loss across all mass flow conditions, particularly near lower flow operating points. For the vane space region of diffuser, the pre- and post-optimization change in total pressure loss is minor, showing decreased loss at lower and increased loss at higher mass flow operating points.

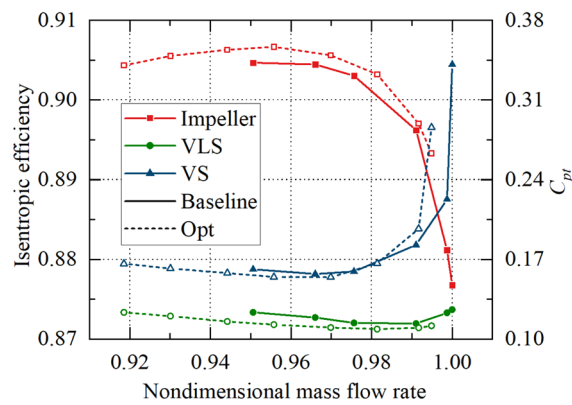


Figure 7. Comparison of the component performance characteristic between baseline and optimization.

The static pressure recovery coefficient is a crucial metric for diffuser performance, representing the ratio of actual to theoretical maximum static pressure increase, as expressed by Equation (5). The main goal of diffuser design is to convert kinetic energy from the fluid at the impeller outlet into potential energy. Both vaneless space and vane space regions have diffusing capabilities, with the vane region notably outperforming the vaneless region. This discrepancy has led to the gradual replacement of vaneless diffusers with vane-type diffusers, especially as centrifugal compressors' pressure ratios have increased over time.

After optimization, the vaneless space region's static pressure recovery coefficient significantly improved, with its diffusing capacity increasing by approximately half, as shown in Figure 8. The vaneless passage expanded after optimization, enlarging the outlet area, as shown in Figure 2. This intensified fluid flow deceleration and subsequent pressure increase, enhancing diffusing capability. Conversely, the vane space region's static pressure recovery coefficient slightly decreased after optimization. Nevertheless, the overall static pressure recovery coefficient of the diffuser, including both vane and vaneless regions, exceeded the original baseline. This indicates that optimization not only preserved the diffuser's diffusing capability but also improved the compressor's operational efficiency.

$$C_{pt} = \frac{P_{t,in} - P_{t,out}}{P_{t,in} - P_{in}} \quad (4)$$

$$C_p = \frac{P_{out} - P_{in}}{P_{t,in} - P_{in}} \quad (5)$$

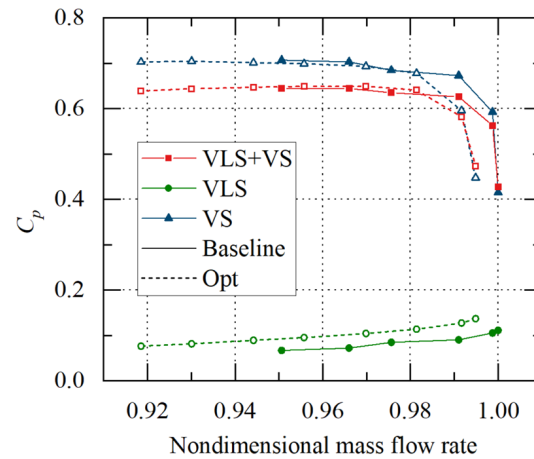


Figure 8. Comparison of the component static pressure recovery coefficient between the baseline and optimization.

3.2. Comparison Peak Efficiency Point

Optimizing the compressor with diffuser hub contouring significantly improved the peak efficiency point. Efficiency improvement is closely related to changes in losses due to the internal flow structure of the compressor. Discussing losses from various flow structures in the compressor is crucial for studying its aerodynamic and thermodynamic processes. According to the second law of thermodynamics, irreversible processes within a system result in a loss of available work and increased entropy production. Losses occur simultaneously with entropy production, so this paper uses entropy production to measure changes in losses. For a control volume, the difference in entropy between the outlet and inlet sections equals the entropy production within the volume. Therefore, the increase in entropy through the components quantitatively measures the losses during the flow process, as definition in Equation (6).

To identify the sources of loss variations in compressor components, the dissipation coefficient is introduced [36]. The dissipation coefficient formula, derived from the Reynolds-averaged Navier–Stokes equations, is as follows. The equation’s right-hand side terms represent entropy production from viscous dissipation and heat transfer under finite temperature gradients. The equation accounts for local velocity gradients, temperature gradients, and turbulence intensity, the main factors deviating the diffuser’s actual thermodynamic processes from isentropic processes. Introducing the dissipation coefficient allows quantitative analysis of losses in various flow structures.

The single-stage centrifugal compressor comprises five components: the inlet region, impeller, VLS, VS, and outlet region, as illustrated in Figure 1. However, the minor contribution of losses in the inlet and outlet regions means their impact on overall efficiency, both before and after optimization, is negligible. Therefore, a separate discussion on these regions is omitted. For loss analysis in this study, the inlet region and impeller are merged into one component, the impeller, and the outlet region and VS are combined as the VS. Thus, the original five components are reclassified and consolidated into three sections.

The diffuser’s flow structure is classified into six categories of losses. The first category is boundary layer loss ($Loss_{bl}$), arising from the high-entropy region generated by the non-slip surfaces of hub, shroud, and vanes. Numerical calculations assume a fully turbulent boundary layer without considering its transition. Given the rapid drop in fluid velocity within the diffuser and the complexity of three-dimensional flow, determining core flow is challenging. Therefore, Y^+ is used to identify the boundary layer, with areas where $Y^+ < 400$ considered as such. Outside the boundary layer, the velocity gradient significantly decreases compared to near the wall. Although this method may introduce error, defining the boundary layer in the diffuser’s three-dimensional compressible flow is challenging. Furthermore, previous studies [37,38] have also used Y^+ as a standard to differentiate the

boundary layer. The second loss category is shock loss ($Loss_{sh}$), where shocks in transonic or supersonic compressors at the impeller and diffuser inlets cause discontinuities in velocity and density, creating a high-entropy region. Density and Mach number gradients classify the shock region. The shock region is defined as an area where both indicators exceed a set standard. The third loss category, recirculation loss ($Loss_{re}$), refers to recirculation flow within the VLS and semi-vaneless space region (SVLS) of the diffuser. This results from large flow angles and inverse pressure gradient that prevent downstream flow, allowing only repetitive flow within this area and causing extra loss. Radial velocity (V_r) < 0 identifies the recirculation region. The fourth loss category, backflow loss ($Loss_{bf}$), occurs when fluid flows in the opposite direction to the core flow within the diffuser channel. The flow direction of the core flow within the diffuser is defined as the mid-curve direction of the wedge vane. Areas where the core flow velocity (V_c) < 0 indicate backflow. The fifth category of loss, vortex loss ($Loss_{vo}$), arises from vortices generated by the fluid's shear force due to viscosity. However, this includes the recirculation and backflow areas, as their flow structures are clearer, as discussed separately. Liu's Ω recognition criterion [39] differentiates the vortex loss region, with $\Omega = 0.52$ as the critical value. The final loss category, mixing loss ($Loss_{mi}$), includes all remaining areas, such as the core flow. Given the complexity of three-dimensional flow, these criteria assess only flow structures with clear characteristics, like $V_c < 0$ in the backflow area. However, even when the backflow area's boundary velocity is 0, the significant speed difference with the core flow leads to mixing and heat transfer, causing loss. This is defined as mixing loss.

The analysis establishes that the compressor's efficiency enhancement is influenced by three components: the impeller, VLS, and VS. Changes in losses for these compressor elements, before and after optimization, are depicted in Figure 9. Assuming the total loss reduction for the compressor is 100%, the VLS shows the largest decline, accounting for 50.2% of the reduction. The VS follows closely, contributing to a 33.6% reduction in losses. In contrast, the impeller shows the smallest change in loss, representing only 16.2% of the total reduction.

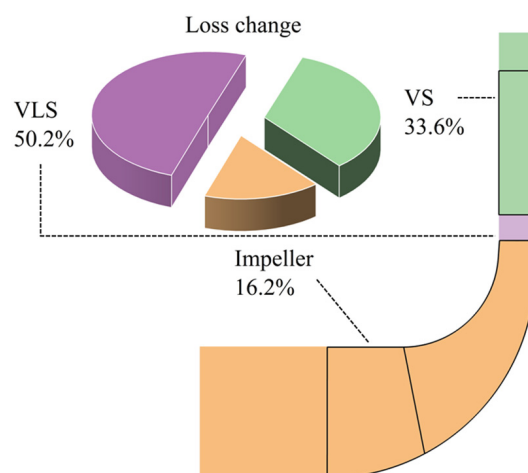


Figure 9. Loss change in different components after optimization at peak efficiency condition.

It is notable that during calculations, fluid intermixing occurs unavoidably at the rotor–stator interface. This intermixing, a numerical result, may lead to an overestimation of losses within the VLS. However, considering losses across the entire diffuser (both the VLS and VS), this deviation's impact is negligible.

$$\begin{aligned}
S &= \frac{\int_A \rho \vec{V} dA}{\int_A \rho \vec{V} dA} \\
\Delta S &= S_{\text{out}} - S_{\text{in}} \\
SC &= \frac{\Delta S}{S_{\text{in}}} \\
\Phi &= \frac{1}{T} \tau_{ij} \frac{\partial u_i}{\partial x_j} + \frac{\lambda}{T^2} \left(\frac{\partial T}{\partial x_j} \right)^2 = \Phi_V + \Phi_T \quad (6) \\
&= \frac{2(\mu + \mu_t) \bar{S}_{ij} \bar{S}_{ij}}{T} + \frac{(\lambda + \lambda_t)}{T^2} \left(\frac{\partial T}{\partial x_j} \right)^2 \\
&= \frac{2\mu \bar{S}_{ij} \bar{S}_{ij}}{T} + \frac{2\mu_t \bar{S}_{ij} \bar{S}_{ij}}{T} + \frac{\lambda}{T^2} \left(\frac{\partial T}{\partial x_j} \right)^2 + \frac{\lambda_t}{T^2} \left(\frac{\partial T}{\partial x_j} \right)^2 \\
&= \Phi_{\bar{V}} + \Phi_{V_t} + \Phi_{\bar{T}} + \Phi_{T_t}
\end{aligned}$$

Optimization of the hub contour of the diffuser significantly influences the flow behavior of the upstream impeller. This change primarily occurs in the impeller's exit region, with the flow near the upstream portion remaining relatively unchanged. Figure 10 illustrates the entropy contour map and streamlines on the meridional plane, after circumferential averaging in a centrifugal compressor stage. Within the impeller, velocity distribution along the span is highly non-uniform, attributed to flow separation, secondary flow, and leakage through blade tip clearances. The baseline compressor shows backflow near the shroud at the impeller exit, coinciding with high-entropy regions within the impeller, as depicted in the figure. This area significantly contributes to loss generation. Optimization results in a more uniform flow field at the impeller outlet, effectively suppressing backflow. As shown in Figure 11, entropy distribution along the span at the optimized impeller outlet shows a significant decrease at over 60% of the span locations. Consequently, the reduction in backflow, more uniform velocity variation along the spanwise, and diminished velocity gradient at the impeller outlet collectively reduce losses. The primary reason for this reduction in losses is the weakened shear effect due to reduced velocity non-uniformity.

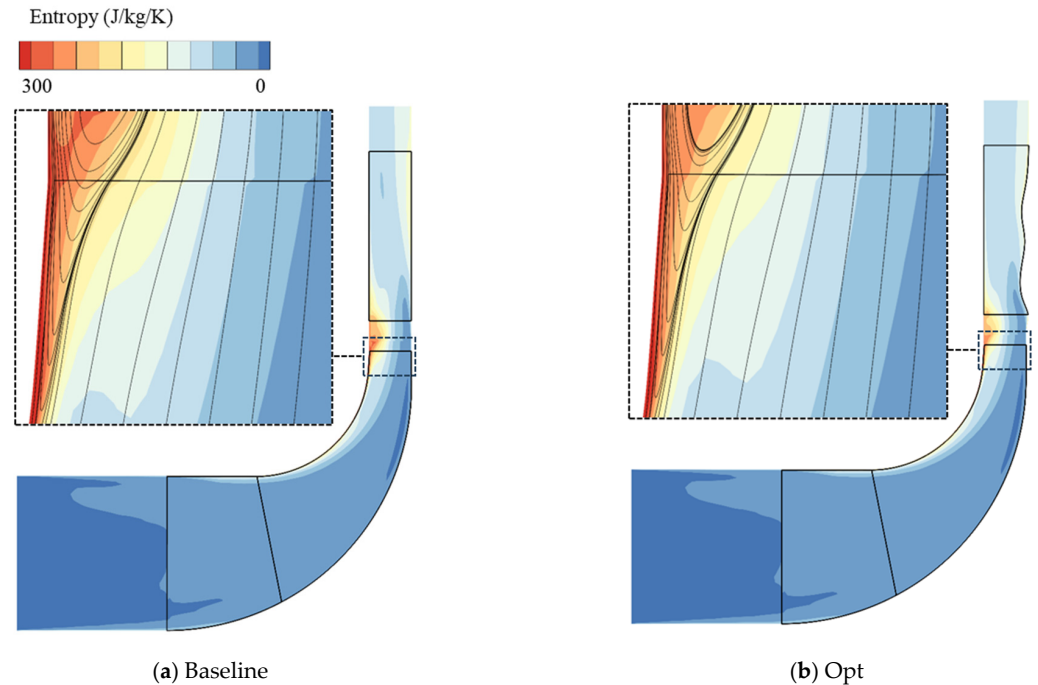


Figure 10. Entropy contour map and streamlines on the meridional plane for a centrifugal compressor stage at peak efficiency condition.

The vaneless region, lacking vanes, features a straightforward flow structure. First, with the expansion of the radius, the meridional channel widens, and the meridional fluid velocity component decreases. Second, without blade forces and frictional effects, the fluid's angular momentum is conserved, reducing the tangential velocity component as

the radius increases. Subsequently, when the hub and shroud of the VLS are parallel, the radial determines the achievable ideal pressure recovery. In this study, the VLS hub was redesigned to show an expanding trend in the optimization results, increasing the diffuser width with radius expansion. Consequently, the ideal pressure recovery of the VLS is jointly determined by the height and radius ratios at the inlet and outlet.

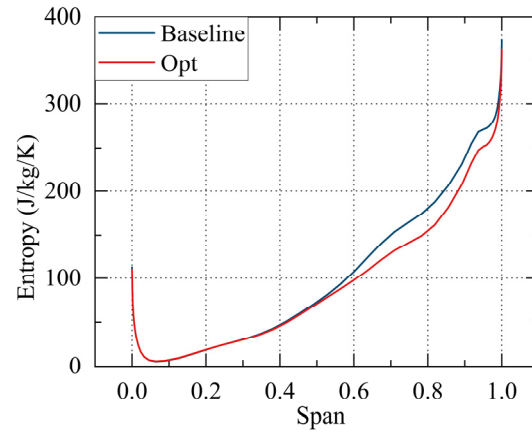
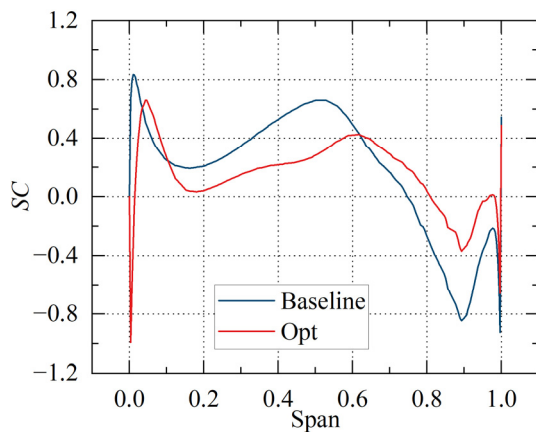


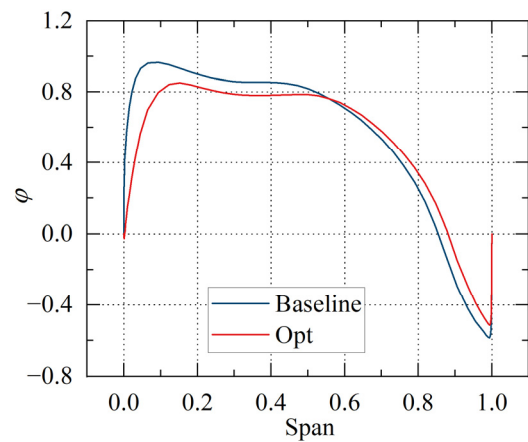
Figure 11. Comparison of entropy distribution spanwise at the impeller outlet between the baseline and the optimization at peak efficiency condition.

Figure 12 shows the spanwise distribution of entropy change and mass flow coefficients at the VLS inlet and outlet. The mass flow coefficient is defined in Equation (7). After optimization, the entropy change coefficient decreases at lower spanwise positions and increases at higher ones. This trend matches the flow coefficient variation, indicating a strong correlation between radial velocity and loss distribution along the span. Expansion of the hub profile results in an increased area ratio at the VLS inlet and outlet, enhancing its pressure recovery capability. Enhanced diffusion within the VLS leads to reduced high-speed flow velocity at lower spanwise positions compared with the baseline and increased radial velocity at higher positions. Additionally, suppression of the recirculation region near the shroud results in a more uniform flow distribution across the span.

$$\varphi = \frac{\rho V_r}{(\rho V_r)_{in}} \tag{7}$$



(a)



(b)

Figure 12. Comparison of entropy change (a) and mass coefficient (b) between baseline and optimization at peak efficiency condition.

Flow losses in the VLS are categorized into recirculation loss, boundary layer loss, and mixing loss, as shown in Figure 13. After optimization, all three types of losses decreased. For the baseline, recirculation flow constituted 16% of the total volume within the VLS, reduced to 15% after optimization. Optimizing the diffuser hub contour effectively suppressed recirculation flow in the vaneless region, reducing this type of loss. The reduction in boundary layer loss after optimization is primarily due to two factors. First, a decrease in core flow velocity led to a thinner boundary layer region. Second, flow passage expansion enhanced deceleration and pressure recovery at the hub, reducing the velocity gradient along the hub's vertical surface and thereby decreasing boundary layer losses. Of the three loss types, mixing loss saw the most significant decrease, accounting for 64% of the total loss reduction in the VLS. The optimized VLS showed a more uniform flow distribution and a reduced recirculation region, leading to a significant decrease in mixing losses between the core flow and low-energy fluid.

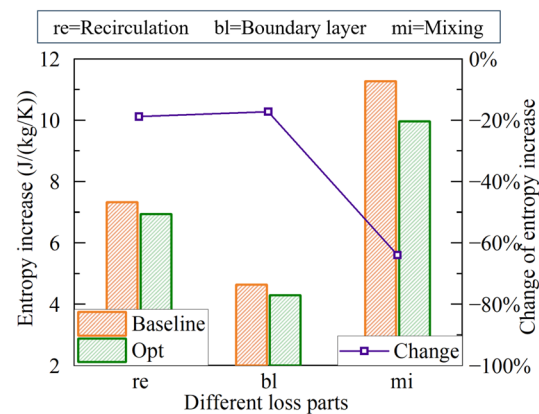


Figure 13. Comparison of VLS entropy increase between baseline and optimization at peak efficiency condition.

The flow characteristics in the VS are intricate, requiring division into two regions: the SVLS and the vane passage (VP) region. Compressor operation stability is affected by SVLS flow dynamics, which will be detailed in subsequent sections. In the SVLS, losses are categorized into six components: backflow, recirculation, boundary layer, shock, vortex, and mixing loss. Changes in these loss components, before and after optimization, are visually depicted in Figure 14. Backflow loss mainly occurs in two regions where flow reverses from downstream to upstream, at the junction between the suction surface and shroud, as illustrated in Figure 15. The white streamlines in the diagram represent the leading edge vortex (A in Figure 15) generated by the vane, due to high incidence angles near the shroud endwall of the vane. The proximity to the shroud causes flow angles in the VLS to exceed 90° , leading to recirculation phenomena. As a result, the SVLS, immediately downstream of the VLS, shows a similar incidence angle phenomenon at a high spanwise location. This large incidence angle causes separation at the leading edge of the vane, worsened by significant losses in corner regions from adverse pressure gradients. Yellow streamline convergence forms throat vorticity (B in Figure 15) near the diffuser's throat region, where the shroud and suction surface meet, with vorticity normal vectors perpendicular to the suction surface of the vane, extending outward. Flow separation in this region is attributed to shock waves, leading to extensive backflow regions along the chord length of the diffuser vane. After optimization, the scale of leading edge separation reduces, and throat vorticity significantly diminishes, as depicted in the diagram. This change is attributed to two main factors. First, reduced incidence angles at high spanwise locations of the diffuser after optimization enhance inlet conditions. Second, the optimized hub meridian line's contraction configuration from the diffuser inlet to the throat reduces adverse pressure gradients in the SVLS, minimizing the likelihood of flow separation.

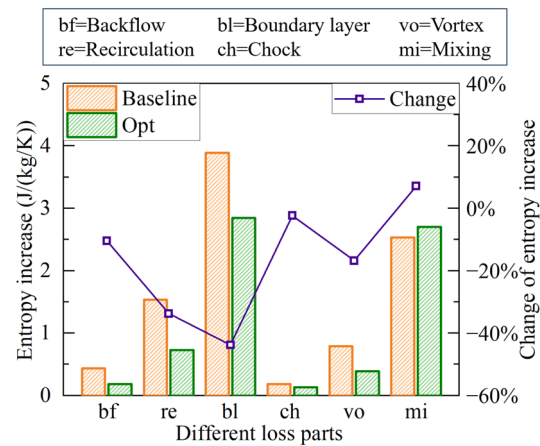


Figure 14. Comparison of SVLS entropy increase between baseline and optimization at peak efficiency condition.

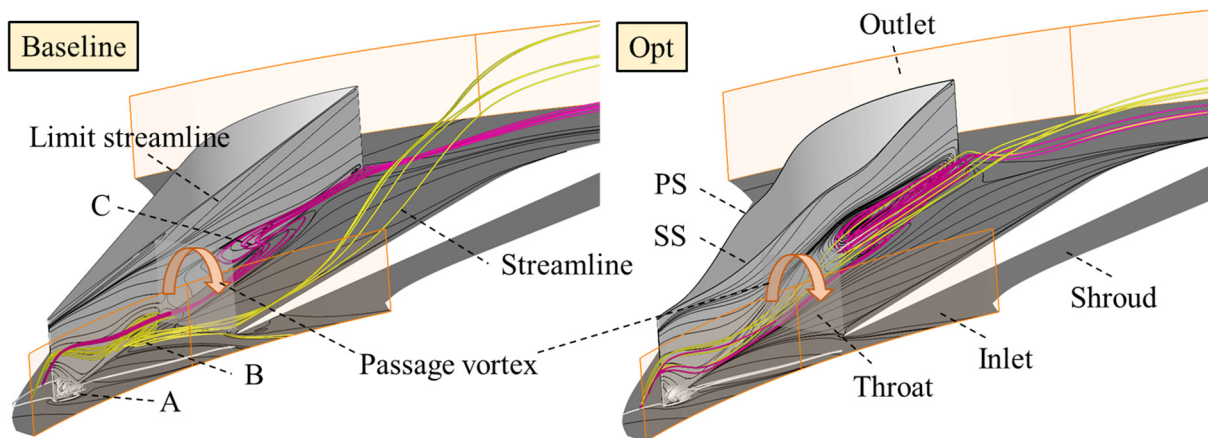


Figure 15. Comparison of flow details in diffuser between baseline and optimization at peak efficiency condition.

Optimization measures resulted in a significant reduction in recirculation losses in the SVLS, the second largest change in loss components, accounting for about 34% of the total changes in this region. Fluid recirculation mainly occurs near high spanwise locations, similar to the VLS recirculation, and depends on the flow angles at the impeller exit. Moreover, pressure variations in the SVLS significantly affect recirculation flow. Reduced diffusion capabilities from optimization increase flow capacity in this region, thereby reducing recirculation tendencies. Changes in boundary layer loss represent the largest reduction in the SVLS losses, amounting for about 44% of the total reduction. The non-uniform radial velocity distribution along the span at the impeller exit creates a significant discrepancy between high and low span positions, with the high-span region having a pronounced positive incidence angle and the low-span region a negative incidence angle at the diffuser inlet. As a result, a clockwise channel vortex forms in the diffuser from the inlet direction, as shown in the diagram. Optimization leads to more uniform flow angle distribution at the diffuser inlet, attenuating the channel vortex's strength and reducing vortex loss. Conversely, changes in shock and mixing loss are negligible.

Losses within the VP are classified and analyzed as shown in Figure 16, excluding the negligible impact of shock waves, contributing only about 0.1% to total losses and not depicted in the figure. After optimization, significant changes result from the hub contour's expansion configuration beyond the throat region, as illustrated in Figure 1. This configuration leads to a more pronounced channel expansion in the region compared with the baseline. The increase in adverse pressure gradient enlarges the existing backflow region (C in Figure 15), leading to increased backflow loss. Downstream flow development in the

VP is accompanied by a gradual thickening of the boundary layer. Backflow regions always appear near the wall surface, with the boundary layer thickness becoming substantial, enough to envelop the entire backflow region. Consequently, a portion of the mixing loss associated with backflow is included within the boundary layer, leading to increased boundary layer loss. Furthermore, reduced flow angles in the VP after optimization contribute to the observed decrease in vortex loss, reflecting changes seen in the SVLS. A more uniform flow angle distribution in the VP attenuates channel vortices' intensity, reducing vortex loss. Remarkably, variation in mixing loss is minimal, with negligible changes before and after optimization. Figure 17 visually represents changes in different loss types within the diffuser before and after optimization. Reductions in recirculation loss and mixing loss are significant, each accounting for about 30% of the total loss reduction in the diffuser. Additionally, reductions in boundary layer and vortex losses contribute about 20% to the diffuser's total loss reduction. Conversely, backflow and shock loss show minimal or no discernible changes before and after optimization.

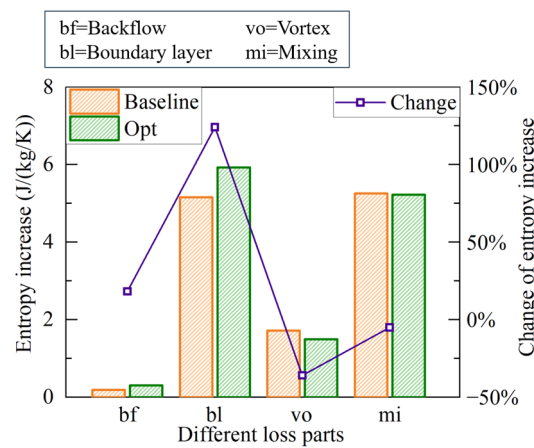


Figure 16. Comparison of VP entropy increase between baseline and optimization at peak efficiency condition.

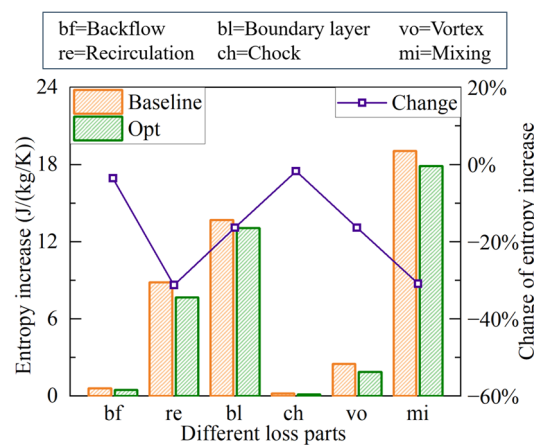


Figure 17. Comparison of different losses in diffuser between baseline and optimization at peak efficiency condition.

The optimized diffuser demonstrates enhanced efficiency and notable advancements in operating margin stability. Examining the near stall point of the baseline and comparing it to the same mass flow operating point after optimization successfully identified factors contributing to the operational range expansion.

As the compressor's mass flow rate decreases, the incidence angle at the diffuser inlet, particularly at high spanwise positions, shows rapid growth at the leading edge of the vane. When the mass flow rate drops below a critical threshold, the diffuser is the first

component in the compressor stage to stall. Figure 18 shows the spatial distribution of radial velocity and incidence angle along the span at the diffuser inlet. As the compressor flow rate diminishes, the region with $V_r < 0$ at the diffuser inlet expands at higher spanwise positions, leading to an increasingly unstable flow within the VLS. Furthermore, radial velocity influences the flow angle at the diffuser inlet. As the flow rate decreases, radial velocity diminishes concurrently. However, with the impeller's constant rotational speed, changes in the tangential velocity component (V_t) are minimal, leading to an increased incidence angle at the diffuser inlet. This increased incidence angle induces flow separation at the leading edge of the diffuser, destabilizing the flow within the SVLS. Previous studies have shown that the VLS and SVLS are critical areas limiting the centrifugal compressor's stability characteristics [33,40–42]. After optimization of the hub contour, the recirculation area at high spanwise positions and the incidence angle at the diffuser inlet significantly decrease, allowing the compressor to operate at a lower mass flow rate.

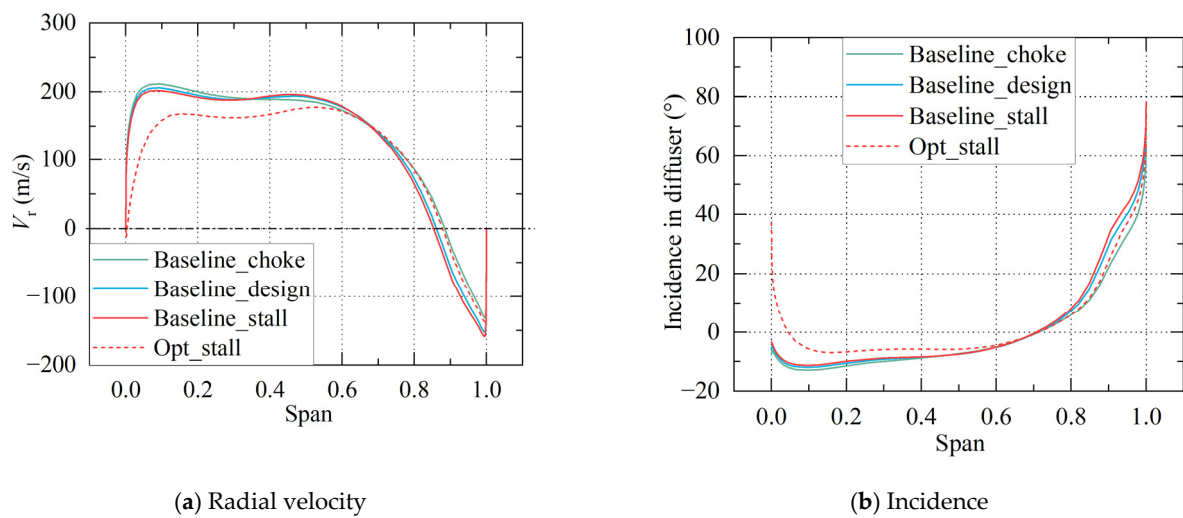


Figure 18. Radial velocity and incidence in the diffuser inlet under different operating conditions.

Statistical analysis was performed on the optimization cases. This investigation examined the correlation between seven design variables and the objective of isentropic efficiency. Spearman's rank coefficient quantifies the relationship between pairs of variables, as expressed in Equation (8). Spearman's rank coefficient ranges between -1 and 1 , with values near these extremes indicating a stronger correlation. In the formula, x_i and y_i are the ranks of the two variables, \bar{x} and \bar{y} are the average ranks of the respective variables, and n is the total number of samples:

$$r = \frac{\sum_{i=1}^n (x_i - \bar{x})(y_i - \bar{y})}{\sqrt{\sum_{i=1}^n (x_i - \bar{x})^2 \sum_{i=1}^n (y_i - \bar{y})^2}} \quad (8)$$

Figure 19 depicts Spearman's rank coefficients between each variable and objective efficiency. All seven variables had coefficients below 0.5, indicating no significant correlation with efficiency. This suggests a complex interplay among design variables collectively influencing objective efficiency, rather than a single key variable impacting compressor efficiency. Comparing Spearman's rank coefficients reveals that the first three variables have higher coefficients, indicating a closer association with the objective function and establishing them as key variables. Furthermore, the geometry of the hub, particularly near the diffuser's upstream region, significantly influences compressor efficiency. Therefore, the design of the VLS and SVLS is critical for enhancing diffuser performance.

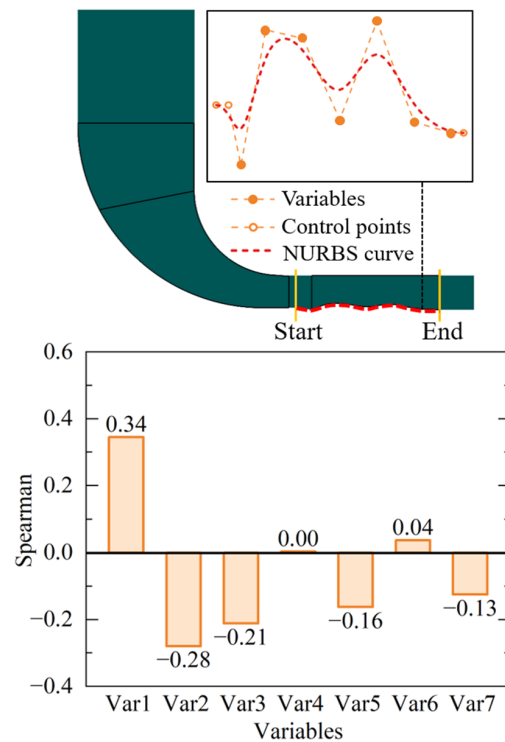


Figure 19. Spearman rank coefficient between variables and isentropic efficiency.

Based on this, a discussion was held about the samples used in the optimization process. In diffusion devices, converting kinetic energy to potential energy is crucial for high efficiency and minimizing work loss. Therefore, Ma is commonly used to measure kinetic energy. This research investigates Ma variations in the diffuser's meridional passage to identify the optimal Ma distribution pattern. The geometric design of the diffuser passage is critical to ensure Ma changes within a reasonable range, preventing flow instabilities and maximizing the pressure recovery coefficient. Specifically, it is desirable for Ma to decrease rapidly within the diffuser, converting more kinetic energy into potential energy. However, if Ma decreases too rapidly, it can cause intense turning and squeezing of fluid within the passage, increasing adverse pressure gradients, and leading to flow separation or backflow, thus increasing flow losses. Therefore, careful geometric design of the diffuser passage is necessary to optimize Ma changes, thereby enhancing system efficiency.

The ideal variation of Ma in the VLS diffusion is a uniform decrease. A linear relationship between Ma and the radial position (R) with a constant slope is desirable for stable, uniform diffusion, reducing losses. Figure 20 shows several optimization cases, Case 1 to Case 4, with peak efficiencies ranging from 79.36% to 81.90%, compared with the baseline peak efficiency of 81.12%. The equation for the optimal Ma distribution in the diffuser's VS is presented as Equation (9).

Here, y represents the nondimensionalized Ma at the diffuser inlet (using mass-averaged Ma), and x denotes the radial position normalized by the inlet radius. Equation (10) represents the partial derivative of the optimal Ma distribution regarding the meridional passage, indicating the Ma distribution slope and explaining the optimal velocity distribution trends. The optimal Ma distribution requires a rapid decrease at the VLS leading edge and a smooth decrease within the VP, aligning with previous findings [43]. However, near the upstream bladeless region, the velocity drop should not be overly rapid, with a slope not smaller than -6.1 . As flow moves downstream, the slope gradually increases. Cases like the baseline, Case 4, and Case 5 show a rapid decrease in velocity at the diffuser inlet, leading to decreased efficiency. Case 5 deviates most from the optimal Ma distribution and has the lowest peak efficiency. These results, combined with correlation analysis, highlight the critical role of the diffuser inlet position in design optimization. The optimal Ma distribution patterns offer

guidance for further diffuser design, but the equation from this study applies only to specific inflow conditions, like transonic and supersonic inflows. When inflow Ma varies, necessary adjustments and optimizations should be made.

$$y = 46.653x^4 - 246.025x^3 + 485.685x^2 - 425.986x + 140.678 \quad (1 < x < 1.49) \quad (9)$$

$$\frac{\partial y}{\partial x} = 186.612x^3 - 738.075x^2 + 971.370x - 425.986 \quad (1 < x < 1.49) \quad (10)$$

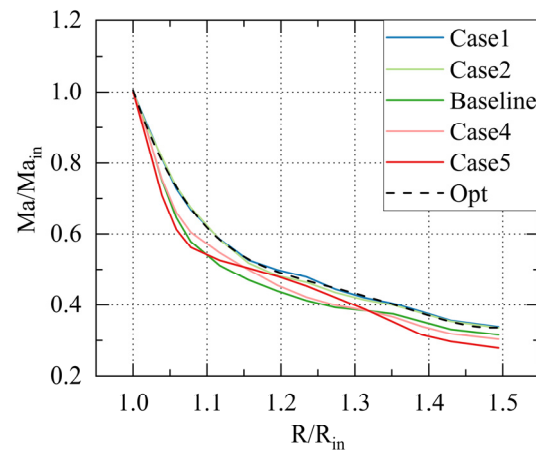


Figure 20. Optimal Ma distribution and Ma distribution in different cases.

4. Conclusions

This study introduces an optimized diffuser hub contour design for a high-pressure ratio centrifugal compressor to enhance peak efficiency. A detailed analysis of losses at the peak efficiency point elucidates the reasons for reduced losses after optimization. Furthermore, flow conditions near the stall point were analyzed to determine the reasons for an expanded stall margin after optimization. Subsequently, a statistical analysis identified key design variables and proposes rules for optimal Mach number distribution in the diffuser. The findings are as follows:

1. The study confirms the feasibility of enhancing centrifugal compressor efficiency and operating range by optimizing the diffuser's hub contour. The optimized centrifugal compressor showed a 0.78% increase in isentropic efficiency and a 7.6% enhancement in the stable operating margin, from 12.8% to 20.4%, compared with the baseline.
2. Optimizing the hub contour significantly affects the centrifugal compressor's diffuser components. Diffuser loss reduction accounts for 83.8% of the compressor's overall loss variation, with 50.2% from the vaneless space and 33.6% from the vane space region. Reductions in recirculation and mixing loss were especially notable in the loss classification.
3. After adopting the optimized hub contour, radial velocity flow distribution in the diffuser's vaneless space becomes more uniform, with decreased flow angles at high spanwise locations. Consequently, recirculation flow suppression in the vaneless and semi-vaneless regions improves compressor stability and enables operation at lower mass flow conditions.
4. Analysis reveals that no individual variable determines the compressor's isentropic efficiency, highlighting the interdependence of variables during optimization. However, the first three variables near the diffuser's leading edge have a greater influence on the compressor's isentropic efficiency.
5. An examination of the Mach number distribution in the diffuser indicates that the Mach number variation at the diffuser inlet significantly impacts efficiency. Under transonic or supersonic inflow conditions of the diffuser, adherence to the provided rules for Mach number distribution in this paper can minimize diffuser losses.

Author Contributions: Conceptualization, Y.W., Z.L. and X.L.; methodology, Q.L., H.Y. and S.Z.; software, Y.W., H.Y. and S.Z.; validation, Y.W., Z.L. and G.H.; formal analysis, Y.W. and Z.L.; investigation, Y.W.; resources, G.H.; data curation, G.H.; writing—original draft preparation, Y.W.; writing—review and editing, Q.L.; visualization, Y.W.; supervision, X.L.; project administration, X.L.; funding acquisition, G.H. and X.L. All authors have read and agreed to the published version of the manuscript.

Funding: This research was funded by the National Natural Science Foundation of China (grant number 52106065) and the National Major Science and Technology Project of China (grant number 2017-II-0002-0014).

Data Availability Statement: The authors confirm that the data supporting the findings of this study are available within the article.

Conflicts of Interest: The authors declare no conflict of interest.

Abbreviations

PS	pressure surface
SS	suction surface
VLS	vaneless space
SVLS	semi-vaneless space
VP	vaned passage
Var	variable
SM	stall margin
π	total pressure ratio
m	mass flow rate
MC	mass flow rate change in choke point
V	velocity
L	work
k	adiabatic coefficient
R	gas constant
η	efficiency
P	pressure
T	temperature
C_{pt}	total pressure loss coefficient
C_p	static pressure recovery coefficient
s	specific entropy
ρ	density
Φ	local dissipation coefficient
τ	friction stress tensor
u	velocity component in cartesian coordinate
λ	thermal conductivity coefficient
\bar{T}	temperature after Reynold average
μ	dynamic viscosity
span	spanwise (from bottom to top of the blade)
r	Spearman rank coefficient

Subscripts

stall	stall condition
design	design condition
Opt	optimization case
t	total parameter
ideal	ideal condition
actual	actual condition
in	inlet
out	outlet
r	radial
c	core

References

1. Krain, H. Review of Centrifugal Compressor's Application and Development. *J. Turbomach.* **2005**, *127*, 25–34. [[CrossRef](#)]
2. Hong, S.; Chi, J.; Xiang, X.; Lu, W. Theoretical Model and Numerical Analysis of the Tip Leakage Vortex Variations of a Centrifugal Compressor. *Aerospace* **2022**, *9*, 830. [[CrossRef](#)]
3. Kenny, D.P. A Novel Low-Cost Diffuser for High-Performance Centrifugal Compressors. *J. Eng. Power* **1969**, *91*, 37–46. [[CrossRef](#)]
4. Casey, M.; Robinson, C. *Radial Flow Turbochargers: Design, Analysis, and Applications*, 1st ed.; Cambridge University Press: Cambridge, UK, 2021; ISBN 978-1-108-24166-3.
5. Yoshinaga, Y.; Gyobu, I.; Mishina, H.; Koseki, F.; Nishida, H. Aerodynamic Performance of a Centrifugal Compressor with Vaned Diffusers. *J. Fluids Eng.* **1980**, *102*, 486–493. [[CrossRef](#)]
6. Abdelwahab, A.; Gerber, G. A new three-dimensional aerofoil diffuser for centrifugal compressors. *Proc. Inst. Mech. Eng. Part A J. Power Energy* **2008**, *222*, 819–830. [[CrossRef](#)]
7. Issac, J.M.; Sitaram, N.; Govardhan, M. Effect of diffuser vane height and position on the performance of a centrifugal compressor. *Proc. Inst. Mech. Eng. Part A J. Power Energy* **2004**, *218*, 647–654. [[CrossRef](#)]
8. Erickson, R.D.; Simon, T.W.; Zhang, L.; Moon, H.-K. *Experimental Investigation of Disc Cavity Leakage Flow and Hub Endwall Contouring in a Linear Rotor Cascade*; American Society of Mechanical Engineers Digital Collection: Washington, DC, USA, 2012; pp. 1769–1780.
9. Civinskas, K.; Povinelli, L. Application of a quasi-3D inviscid flow and boundary layer analysis to the hub-shroud contouring of a radial turbine. In Proceedings of the 20th Joint Propulsion Conference, Cincinnati, OH, USA, 11–13 June 1984; American Institute of Aeronautics and Astronautics: Wriston, VA, USA, 1984.
10. Kopper, F.C.; Milano, R.; Vanco, M. Experimental Investigation of Endwall Profiling in a Turbine Vane Cascade. *AIAA J.* **1981**, *19*, 1033–1040. [[CrossRef](#)]
11. Burd, S.W.; Simon, T.W. Flow Measurements in a Nozzle Guide Vane Passage with a Low Aspect Ratio and Endwall Contouring. *J. Turbomach.* **2000**, *122*, 659–666. [[CrossRef](#)]
12. Dossena, V.; Perdichizzi, A.; Savini, M. The Influence of Endwall Contouring on the Performance of a Turbine Nozzle Guide Vane. *J. Turbomach.* **1999**, *121*, 200–208. [[CrossRef](#)]
13. Duden, A.; Raab, I.; Fottner, L. Controlling the Secondary Flow in a Turbine Cascade by Three-Dimensional Airfoil Design and Endwall Contouring. *J. Turbomach.* **1999**, *121*, 191–199. [[CrossRef](#)]
14. Bohn, D.E.; Kusterer, K.; Sürken, N.; Kreitmeier, F. *Influence of Endwall Contouring in Axial Gaps on the Flow Field in a Four-Stage Turbine*; American Society of Mechanical Engineers Digital Collection: Washington, DC, USA, 2014.
15. Ito, Y.; Watanabe, T.; Himeno, T. Effect of Endwall Contouring on Flow Instability of Transonic Compressor. *Int. J. Gas Turbine Propuls. Power Syst.* **2008**, *2*, 24–29. [[CrossRef](#)]
16. Kroger, G.; Voß, C.; Nicke, E.; Cornelius, C. Theory and Application of Axisymmetric Endwall Contouring for Compressors. In Proceedings of the Volume 7: Turbomachinery, Parts A, B, and C, Vancouver, BC, Canada, 6–10 June 2011; ASMEDC: Washington, DC, USA, 2011; pp. 125–137.
17. Kröger, G.; Cornelius, C.; Nicke, E. Rotor Casing Contouring in High Pressure Stages of Heavy Duty Gas Turbine Compressors with Large Tip Clearance Heights. In Proceedings of the Volume 7: Turbomachinery, Parts A and B, Orlando, FL, USA, 8–12 June 2009; ASMEDC: Washington, DC, USA, 2009; pp. 215–225.
18. Hoeger, M.; Cardamone, P.; Fottner, L. *Influence of Endwall Contouring on the Transonic Flow in a Compressor Blade*; American Society of Mechanical Engineers Digital Collection: Washington, DC, USA, 2009; pp. 759–768.
19. Chen, P.-P.; Qiao, W.-Y.; Hashmi, S.F.A.; Shi, P.-J.; Zhao, L. Passive control of hub-corner separation/stall using axisymmetric-hub contouring. *Proc. Inst. Mech. Eng. Part G J. Aerosp. Eng.* **2012**, *226*, 1214–1224. [[CrossRef](#)]
20. Sun, S.; Chen, S.; Liu, W.; Gong, Y.; Wang, S. Effect of axisymmetric endwall contouring on the high-load low-reaction transonic compressor rotor with a substantial meridian contraction. *Aerosp. Sci. Technol.* **2018**, *81*, 78–87. [[CrossRef](#)]
21. Han, G.; Yang, C.; Zhao, S.; Zhang, Y.; Lu, X. Investigation of a High Pressure Ratio Centrifugal Compressor with Wedge Diffuser and Pipe Diffuser. *Int. J. Turbo Jet-Engines* **2021**, *38*, 1–13. [[CrossRef](#)]
22. Wang, X.-F.; Xi, G.; Wang, Z.-H. Aerodynamic optimization design of centrifugal compressor's impeller with Kriging model. *Proc. Inst. Mech. Eng. Part A J. Power Energy* **2006**, *220*, 589–597. [[CrossRef](#)]
23. Ha, K.K.; Kang, S.H. An Optimization Method for Centrifugal Compressor Design Using the Surrogate Management Framework. In Proceedings of the ASME-JSME-KSME 2011 Joint Fluids Engineering Conference: Volume 1, Symposia—Parts A, B, C, and D, Hamamatsu, Japan, 24–29 July 2011; ASMEDC: Washington, DC, USA, 2011; pp. 679–684.
24. Ji, C.; Wang, Z.; Xi, G. Computer 3D Vision-Aided Full-3D Optimization of a Centrifugal Impeller. *J. Turbomach.* **2022**, *144*, 091011. [[CrossRef](#)]
25. Shaaban, S. Design optimization of a centrifugal compressor vaneless diffuser. *Int. J. Refrig.* **2015**, *60*, 142–154. [[CrossRef](#)]
26. Sakaguchi, D.; Tun, M.; Numakura, R.; Wang, B. Global optimization of recirculation flow type casing treatment in centrifugal compressors of turbochargers. *Proc. Inst. Mech. Eng. Part C J. Mech. Eng. Sci.* **2018**, *232*, 4461–4471. [[CrossRef](#)]
27. Liu, S.; Geng, S.; Li, X.; Jin, Y.; Zhang, H. Optimization Design of Aspect Ratio and Solidity of a Heavy-Duty Gas Turbine Transonic Compressor Rotor. *Machines* **2023**, *11*, 82. [[CrossRef](#)]
28. Ekradi, K.; Madadi, A. Performance improvement of a transonic centrifugal compressor impeller with splitter blade by three-dimensional optimization. *Energy* **2020**, *201*, 117582. [[CrossRef](#)]

29. Kim, J.-H.; Choi, J.-H.; Kim, K.-Y. Surrogate Modeling for Optimization of a Centrifugal Compressor Impeller. *Int. J. Fluid Mach. Syst.* **2010**, *3*, 29–38. [[CrossRef](#)]
30. Lang, J.; Chu, W.; Spence, S.; An, G.; Galloway, L. Performance enhancement of a centrifugal compressor stage using profiled end wall (PEW) treatments in the radial vaned diffuser. *Aerosp. Sci. Technol.* **2021**, *110*, 106488. [[CrossRef](#)]
31. Dutton, J.C.; Piemsomboon, P.; Jenkins, P.E. Flowfield and Performance Measurements in a Vaned Radial Diffuser. *J. Fluids Eng.* **1986**, *108*, 141–147. [[CrossRef](#)]
32. Everitt, J.N.; Spakovszky, Z.S. An Investigation of Stall Inception in Centrifugal Compressor Vaned Diffuser1. *J. Turbomach.* **2013**, *135*, 011025. [[CrossRef](#)]
33. Hunziker, R.; Gyarmathy, G. The Operational Stability of a Centrifugal Compressor and Its Dependence on the Characteristics of the Subcomponents. *J. Turbomach.* **1994**, *116*, 250–259. [[CrossRef](#)]
34. Zheng, X.; Lin, Y.; Gan, B.; Zhuge, W.; Zhang, Y. Effects of Reynolds number on the performance of a high pressure-ratio turbocharger compressor. *Sci. China Technol. Sci.* **2013**, *56*, 1361–1369. [[CrossRef](#)]
35. Tiainen, J.; Jaatinen-Värri, A.; Grönman, A.; Backman, J. *Numerical Study of the Reynolds Number Effect on the Centrifugal Compressor Performance and Losses*; American Society of Mechanical Engineers Digital Collection: Washington, DC, USA, 2016; p. V02DT42A002.
36. Li, Z.; Lu, X.; Wu, Y.; Cheng, H.; Han, G. Thermodynamic investigation of the secondary flow inside centrifugal compressor for compressed air energy storage based on local dissipation. *J. Energy Storage* **2023**, *74*, 109325. [[CrossRef](#)]
37. Zaripov, D.; Li, R.; Dushin, N. Dissipation rate estimation in the turbulent boundary layer using high-speed planar particle image velocimetry. *Exp. Fluids* **2019**, *60*, 18. [[CrossRef](#)]
38. Li, Z.; Lu, X.; Wu, Y.; Han, G. Quantitative investigation of the turbulence model effect on high-pressure-ratio centrifugal compressor performance prediction. *Int. Commun. Heat Mass Transf.* **2023**, *142*, 106644. [[CrossRef](#)]
39. Liu, C.; Wang, Y.; Yang, Y.; Duan, Z. New omega vortex identification method. *Sci. China Phys. Mech. Astron.* **2016**, *59*, 684711. [[CrossRef](#)]
40. Ferrara, G.; Ferrari, L.; Mengoni, C.P.; De Lucia, M.; Baldassarre, L. Experimental Investigation and Characterization of the Rotating Stall in a High Pressure Centrifugal Compressor: Part I—Influence of Diffuser Geometry on Stall Inception. In Proceedings of the Volume 5: Turbo Expo 2002, Parts A and B, Amsterdam, The Netherlands, 3–6 June 2002; ASME/EDC: Washington, DC, USA, 2002; pp. 613–620.
41. Zhang, Y.; Lu, X.; Zhang, Y.; Zhang, Z.; Dong, X.; Han, G. Stall Behavior in an Ultrahigh-Pressure-Ratio Centrifugal Compressor: Backward-Travelling Rotating Stall. *J. Turbomach.* **2022**, *144*, 101010. [[CrossRef](#)]
42. Fujisawa, N.; Inui, T.; Ohta, Y. Evolution Process of Diffuser Stall in a Centrifugal Compressor with Vaned Diffuser. *J. Turbomach.* **2019**, *141*, 041009. [[CrossRef](#)]
43. Li, Q.; Sun, Z.; Lu, X.; Zhang, Y.; Han, G. Investigation of New Design Principles for the Centrifugal Compressor Vaned Diffusers. *Int. J. Aerosp. Eng.* **2022**, *2022*, 4480676. [[CrossRef](#)]

Disclaimer/Publisher’s Note: The statements, opinions and data contained in all publications are solely those of the individual author(s) and contributor(s) and not of MDPI and/or the editor(s). MDPI and/or the editor(s) disclaim responsibility for any injury to people or property resulting from any ideas, methods, instructions or products referred to in the content.